Title
Modeling C1–C4 Alkyl Nitrate Photochemistry and Their Impacts on O3 Production in Urban and Suburban Environments of Hong Kong

Journal
Journal of Geophysical Research: Atmospheres, 122(19)

ISSN
2169-897X

Authors
Lyu, XP
Guo, H
Wang, N
et al.

Publication Date
2017-10-16

DOI
10.1002/2017JD027315

AGU PUBLICATIONS

JGR

Journal of Geophysical Research: Atmospheres

RESEARCH ARTICLE
10.1002/2017JD027315

Key Points:
- A PBM-MCM model was developed to simulate gas-phase $RONO_2$ measured at an urban and a mountainous site in Hong Kong
- $RONO_2$ formation depended upon not only the abundances of precursors but also the photochemical reactivity
- $RONO_2$ degradation influencing O_3 production included NO_2 stimulating, NO_2 suppressing, and RO stimulating processes

Supporting Information:
- Supporting Information S1

Correspondence to:
H. Guo and H. R. Cheng,
ceguohai@polyu.edu.hk;
chenghr@whu.edu.cn

Citation:
Lyu, X. P., Guo, H., Wang, N., Simpson, I. J., Cheng, H. R., Zeng, L. W., … Blake, D. R. (2017). Modeling C_1–C_4 alkyl nitrate photochemistry and their impacts on O_3 production in urban and suburban environments of Hong Kong. *Journal of Geophysical Research: Atmospheres*, *122*, 10,539–10,556. https://doi.org/10.1002/2017JD027315

Received 20 JUN 2017
Accepted 22 SEP 2017
Accepted article online 26 SEP 2017
Published online 14 OCT 2017

Modeling C_1–C_4 Alkyl Nitrate Photochemistry and Their Impacts on O_3 Production in Urban and Suburban Environments of Hong Kong

X. P. Lyu[1,2], H. Guo[1,2], N. Wang[3], I. J. Simpson[4], H. R. Cheng[5], L. W. Zeng[1,2], S. M. Saunders[6], S. H. M. Lam[6,7], S. Meinardi[4], and D. R. Blake[4]

[1]Department of Civil and Environmental Engineering, Hong Kong Polytechnic University, Hong Kong, [2]Research Institute for Sustainable Urban Development, Hong Kong Polytechnic University, Hong Kong, [3]Guangdong Provincial Key Laboratory of Regional Numerical Weather Prediction, Institute of Tropical and Marine Meteorology, Guangzhou, China, [4]Department of Chemistry, University of California, Irvine, CA, USA, [5]Department of Environmental Engineering, School of Resource and Environmental Sciences, Wuhan University, Wuhan, China, [6]School of Chemistry and Biochemistry, University of Western Australia, Perth, Western Australia, Australia, [7]Pacific Environment Limited, Perth, Western Australia, Australia

Abstract As intermediate products of photochemical reactions, alkyl nitrates ($RONO_2$) regulate ozone (O_3) formation. In this study, a photochemical box model incorporating master chemical mechanism well reproduced the observed $RONO_2$ at an urban and a mountainous site, with index of agreement in the range of 0.66–0.73. The value 0.0003 was identified to be the most appropriate branching ratio for C_1 $RONO_2$, with the error less than 50%. Although levels of the parent hydrocarbons and nitric oxide (NO) were significantly higher at the urban site than the mountainous site, the production of C_2–C_3 $RONO_2$ was comparable to or even lower than at the mountainous site, due to the lower concentrations of oxidative radicals in the urban environment. Based on the profiles of air pollutants at the mountainous site, the formation of C_2–C_4 $RONO_2$ was limited by NO_x (volatile organic compounds (VOCs)) when total volatile organic compounds (TVOCs)/NO_x was higher (lower) than 10.0 ± 0.4 parts per billion by volume (ppbv)/ppbv. This dividing ratio decreased ($p < 0.05$) to 8.7 ± 0.4 ppbv/ppbv at the urban site, mainly due to the different air pollutant profiles at the two sites. For the formation of C_1 $RONO_2$, the NO_x-limited regime extended the ratio of TVOCs/NO_x to as low as 2.4 ± 0.2 and 3.1 ± 0.1 ppbv/ppbv at the mountainous and urban site, respectively. $RONO_2$ formation led to a decrease of simulated O_3, with reduction efficiencies (O_3 reduction/$RONO_2$ production) of 4–5 parts per trillion by volume (pptv)/pptv at the mountainous site and 3–4 pptv/pptv at the urban site. On the other hand, the variations of simulated O_3 induced by $RONO_2$ degradation depended upon the regimes controlling O_3 formation and the relative abundances of TVOCs and NO_x.

1. Introduction

Alkyl nitrates ($RONO_2$) are a group of organic nitrates in which the nitrogen is stabilized in the molecular structure of R-O-NO_2. As an important constituent of reactive odd nitrogen (NO_y), particularly in areas far from urban sources (Buhr et al., 1990; Roberts & Fajer, 1989), $RONO_2$ participate in nitrogen cycling in their role as a temporary nitrogen reservoir (Clemitshaw et al., 1997). Generally, oceanic emission (Atlas et al., 1993), photochemical formation (Arey et al., 2001; Bertman et al., 1995), and to a lesser extent biomass burning (Simpson et al., 2002) are the main sources of $RONO_2$. The photochemically formed $RONO_2$ are actually by-products in the process of O_3 formation and are formed through the reactions between volatile organic compounds (VOCs) and nitrogen oxides (NO_x). These combined formation pathways, as a result, generally lead to the tight association between $RONO_2$ and O_3 (Muthuramu et al., 1994; Rosen et al., 2004).

Many formation mechanisms have been proposed to explain observed $RONO_2$ levels in urban settings, including RO_2 reacting with NO (Carter & Atkinson, 1989; Darnall et al., 1976) and RO reacting with NO_2 (Atkinson et al., 1982), which are well documented and play dominant roles in $RONO_2$ formation, particularly in daytime hours. For the reactions of RO_2 + NO, two branches exist, leading to the formation of $RONO_2$ (R1) and O_3 (R2), respectively (Atkinson, 1990). The branching ratio (α) is a quantitative measure of $RONO_2$ yield from RO_2 reacting with NO. It is defined as the ratio of $k_1/(k_1 + k_2)$ (Atkinson, 1990), where k is the reaction rate constant. Generally, the branching ratio increases with increasing pressure and decreasing temperature (Atkinson et al., 1987). In addition, more complicated molecular structures of RO_2 tend to have higher

branching ratios. For example, the branching ratios for *n*-alkanes increase from ≤1% for ethane to ~33% for *n*-octane, with an upper limit of ~35% for larger *n*-alkanes (Atkinson et al., 1982). This theory was repeatedly confirmed by kinetic calculations and model simulations (Bertman et al., 1995; Simpson et al., 2006). In combination with laboratory studies, Carter and Atkinson (1985, 1989) proposed formulas (1)–(3) for calculating branching ratios under the atmospheric conditions in the troposphere. According to the calculations, the branching ratio of the methyl peroxy radical (CH_3O_2) was approximately 0.001 in the lower stratosphere and 0.003 in the lower troposphere. This suggests that the branching ratio of CH_3O_2 at the surface could also be acquired by applying a correction factor of ~3 to the branching ratio in lower stratosphere. In contrast to theoretical calculations, the smaller-chain $RONO_2$, particularly methyl (CH_3ONO_2) and ethyl nitrate ($C_2H_5ONO_2$), often have mixing ratios higher than what can be explained by the reaction of RO_2 with NO in urban environments (Flocke, Volz-Thomas et al., 1998). Depending on the location, direct marine emissions could be one reason (Atlas et al., 1993). In addition, the exact branching ratios for these $RONO_2$ remain uncertain. For example, Lightfoot et al. (1992) proposed an upper limit of 0.005 for CH_3ONO_2 in the lower troposphere. However, through $RONO_2$ observations in the lower stratosphere, Flocke, Atlas et al. (1998) found a much lower CH_3ONO_2 branching ratio of $5–10 \times 10^{-5}$, meaning it could only reach a maximum of 0.0003 even under surface conditions, when applying the adjusted factor of 3 to the branching ratio in lower stratosphere. Simpson et al. (2006) accepted the upper limit of 0.0003 and indicated that RO reacting with NO_2 was the main pathway of CH_3ONO_2 in highly polluted environments. Fewer studies on the branching ratios of C_2–C_4 $RONO_2$ have been conducted. Based on laboratory experiments at 299 ± 2°K and 735 torr, 1982 found that the branching ratios for RO_2 forming $RONO_2$ following the oxidation of ethane, propane and *n*-butane were ≤0.014, 0.036 ± 0.005, and 0.077 ± 0.009, respectively. For primary RO_2 radicals, the branching ratios might be lower by a factor of 2 (Ranschaert et al., 2000). However, the branching ratios for $RONO_2$ formation remain to be further examined.

R1 $$RO_2 + NO \rightarrow RONO_2 \quad (k_1)$$

R2 $$RO_2 + NO \rightarrow RO + NO_2 \quad (k_2)$$

R3 $$NO_2 + O_2 \rightarrow NO + O_3 \quad (k_3)$$

R4 $$RO + NO_2 \rightarrow RONO_2 \quad (k_4)$$

$$\alpha = \left[\frac{Y_0^{300}[M]\left(\frac{T}{300}\right)^{-m_0}}{1 + \frac{Y_0^{300}[M]\left(\frac{T}{300}\right)^{-m_0}}{Y_\infty^{300}\left(\frac{T}{300}\right)^{-m_\infty}}}\right] F^z \tag{1}$$

$$z = \left\{1 + \left[\log\frac{Y_0^{300}[M]\left(\frac{T}{300}\right)^{-m_0}}{Y_\infty^{300}\left(\frac{T}{300}\right)^{-m_\infty}}\right]^2\right\}^{-1} \tag{2}$$

$$Y_0^{300} = \beta e^{\gamma n} \tag{3}$$

where T is the temperature (K), M represents the number of molecules (molecules/cm^3), and n is the carbon number in RO_2. The values of the constants β (1.95×10^{-22} cm^3/molecule), γ (0.947), Y_∞^{300} (0.435), m_0 (2.99), m_∞ (4.69), and F (0.556) are all from Carter and Atkinson (1985). On the basis of the calculated results, the branching ratios for the primary and tertiary RO_2 radicals are calibrated by a factor of 0.4 and 0.25, respectively.

It is well known that O_3 formation is closely related to the relative abundances of VOCs and NO_x, mainly due to the dual role of NO_x in O_3 production (i.e., fueling and suppressing O_3 formation in low and high NO_x regimes, respectively) (Shao et al., 2009; Sillman & He, 2002). As by-products of O_3 formation, the production of $RONO_2$ is also expected to be influenced by the abundances of VOCs and NO_x. In brief, NO reacts with the hydroperoxyl radical (HO_2) and RO_2, and NO_2 combines with hydroxyl radical (OH), regulating the equilibrium budgets of oxidative radicals including RO_2 and RO (Thornton et al., 2002). As such, the $RONO_2$ production will also be influenced by NO_x, similar to O_3. It was found that $RONO_2$ levels increased with increasing NO_x in London

(Aruffo et al., 2014). However, in Houston $RONO_2$ and other nitrogen-containing species except for NO_x were found to increase during the decrease of NO_y (Rosen et al., 2004), indicating the anticorrelation between $RONO_2$ and NO_x. This might imply the NO_x-limited (e.g., London) and VOC-limited regime (e.g., Houston) in $RONO_2$ formation. Therefore, the relationship between $RONO_2$ production and NO_x needs further study.

Due to the associated formation pathways of $RONO_2$ and O_3, good correlations are often found between single or total $RONO_2$ (∑ANs) and O_3 or O_x ($O_x = O_3 + NO_2$) (Perring et al., 2010; Rosen et al., 2004). A roughly quantitative relationship can be established between O_x and ∑ANs, that is, $O_x/\sum ANs = 2(1-\alpha)/\alpha$ (Day et al., 2003), where α represents the overall branching ratio for the total $RONO_2$. More importantly, $RONO_2$ photochemistry, including their formation and degradation (photolysis- and OH-initiated oxidation) also influences O_3 formation. Based on correlations between O_x and ∑ANs, Aruffo et al. (2014) stated that $RONO_2$ played important roles in O_3 formation in both urban and suburban London. Perring et al. (2010) indicated that the peak O_3 production in the near field of Mexico City (source region of $RONO_2$) was reduced by as much as 40% due to the formation of total $RONO_2$. Farmer et al. (2011) even claimed that VOC reductions might cause an O_3 increment because the branching ratios of $RONO_2$ formation decreased when fuels containing low boiling point VOCs products were used. This view was also held by Perring et al. (2013), who estimated a theoretical 8% O_3 increment even under VOCs reduction of 20%, due to the unexpected decrease of the average branching ratio for total $RONO_2$ from 8% to 4%. Overall, in urban areas $RONO_2$ serve as a reservoir for nitrogen and reactive radicals, releasing them in remote areas and fueling O_3 formation. Therefore, $RONO_2$ photochemistry regulates O_3 formation in both source and receptor regions.

Despite numerous studies, $RONO_2$ modeling is still rather difficult (Khan et al., 2015; Williams et al., 2014), resulting in an insufficient understanding of $RONO_2$ formation mechanisms and impacts on O_3 production. Furthermore, previous studies (Rosen et al., 2004; Sobanski et al., 2016) focused on measuring the combined sum of all alkyl nitrates, rather than matching multiple $RONO_2$ species as attempted by this study. To fill in these research gaps, an observation-based model was constructed to near-explicitly simulate C_1–C_4 $RONO_2$ in Hong Kong and address the following terms: (1) the most appropriate branching ratios for the formation of C_1–C_4 $RONO_2$ in Hong Kong, (2) the pathway contributions of $RO_2 + NO$ and $RO + NO_2$ to $RONO_2$, (3) the relationship between $RONO_2$ production and their precursors (i.e. VOCs and NO_x), and (4) the impacts of $RONO_2$ formation and degradation on O_3 production.

2. Methodology

2.1. Site Description and Sampling

From 6 September to 29 November 2010, an intensive sampling campaign was carried out concurrently at a mountainous site and an urban site in Hong Kong (Figure 1). The mountainous site (22.41°N, 114.12°E, 640 m above ground level (agl)) was located on the mountainside of Hong Kong's highest mountain (Mount Tai Mo Shan), referred to as TMS hereafter. The dominant winds at TMS were from the north that transported air pollutants from the inland Pearl River Delta (PRD) of southern China. In addition, mesoscale circulation (e.g., mountain-valley breezes) caused interaction of mountainous air with urban plumes at the foot of the mountain. The urban site (22.37°N, 114.11°E, 10 m agl) is located in a newly developed town (Tsuen Wan, referred to as TW hereafter) and is an air quality monitoring station of Hong Kong Environmental Protection Department (HKEPD, accessible at http://www.aqhi.gov.hk/en/monitoring-network/air-quality-monitoring-stations228e.html?%20stationid=77). The prevailing winds at TW were from the southeast. Detailed information about the two sites is given in Guo et al. (2013) and Ling et al. (2014, 2016).

Real time measurements of trace gases including SO_2, CO, NO, NO_2, and O_3 at TMS were achieved with the instruments listed in Table S1 in the supporting information, which also shows the analytical techniques, detection limits, and precision. Trace gas data at TW were downloaded from the HKEPD website (http://epic.epd.gov.hk/EPICDI/air/station/). VOC samples at these two sites were collected using 2 L electropolished stainless steel canisters. Prior to sampling, the canisters were treated with 10 torr of degassed, distilled water to quench the active surface sites of the inner walls and then were cleaned and evacuated. A valve was connected to the inlet of the canisters to maintain a sampling time of about 1 h. A total of 384 samples was simultaneously collected in daytimes of 10 O_3 episode days (23–24 and 29–31 October and 1–3, 9, and 19 November 2010) and 10 non-O_3 episode days (28 September, 2, 8, 14, 18–19, and 27–28 October,

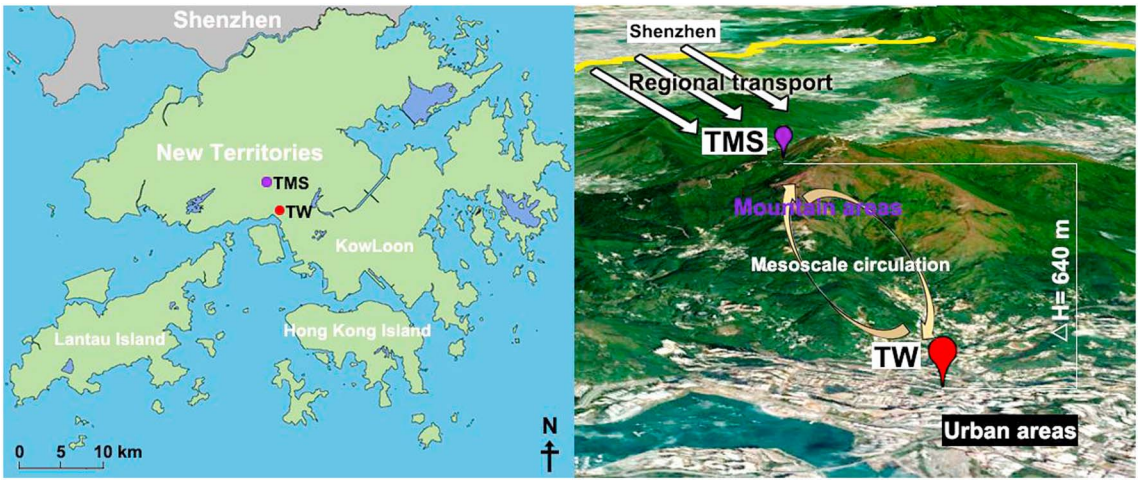

Figure 1. Geographic (left) locations and (right) topographies of the sampling sites (TMS and TW). Regional transport and mesoscale circulation at TMS are presented according to Guo et al. (2013). The boundary between mainland China and Hong Kong is highlighted in yellow.

and 20–21 November 2010) at TMS and TW, except those samples not collected at TW on October 23. Samples were collected at 21:00, 0:00, and 3:00 and at each hour from 7:00 to 19:00 during O_3 episodes, while they were collected every 2 h from 07:00 to 19:00 on non-O_3 episode days. In this study, days with at least 1-hourly O_3 mixing ratio exceeding 100 ppbv were defined as O_3 episode days (China's Grade II standards, accessible at http://210.72.1.216:8080/gzaqi/Document/gjzlbz.pdf). The O_3 values at TMS were used to define the O_3 episodes and nonepisodes, because freshly emitted NO from vehicular exhaust strongly titrated O_3 at TW (Guo et al., 2013).

2.2. Chemical Analysis of $RONO_2$

The collected VOC samples were delivered to the Rowland/Blake group at the University of California, Irvine (UCI), for chemical analyses. Detailed descriptions about the analytical system, analysis techniques, precision, accuracy, and quality control protocols can be found in Colman et al. (2001) and Simpson et al. (2006).

Specifically, for the quantification of C_1–C_4 $RONO_2$, that is, methyl nitrate (CH_3ONO_2 or C_1 $RONO_2$), ethyl nitrate ($C_2H_5ONO_2$ or C_2 $RONO_2$), *i*-propyl nitrate (2-$C_3H_7ONO_2$ or 2-C_3 $RONO_2$), *n*-propyl nitrate (1-$C_3H_7ONO_2$ or 1-C_3 $RONO_2$), and *sec*-butyl nitrate (2-$C_4H_9ONO_2$ or 2-C_4 $RONO_2$), a gas chromatography-electron capture detector system was used. Two whole air working standards were analyzed every four samples to calibrate the $RONO_2$ measurements. The precision was 2% for mixing ratios above 5 parts per trillion by volume (pptv) and 10% for mixing ratios below 5 pptv. The accuracy was 10–20%, and the detection limit for C_1–C_4 $RONO_2$ was 0.01 pptv. It is worth noting that the $RONO_2$ calibration scale changed in 2008 (Simpson et al., 2011) and all measurements are reported on the new calibration scale.

2.3. Construction of PBM-MCM Model

A photochemical box model-master chemical mechanism (PBM-MCM) model was developed to simulate $RONO_2$. Master chemical mechanism (MCM) is an explicit chemical mechanism, which has been successfully used in photochemical simulation in Hong Kong and many other regions of the world (Lam et al., 2013; Ling et al., 2014; Saunders et al., 2003). The latest version of MCM (MCM v3.3) includes 17,242 reactions and 5,836 species (Jenkin et al., 2015). Reactions of biogenic VOCs including limonene and myrcene, and $RONO_2$ were added into MCM by our team. In particular, the model describes reactions of more than 100 $RONO_2$ species. The main formation pathways of $RONO_2$ that are considered are RO_2 + NO and RO + NO_2, while $RONO_2$ degradation is presented as photolysis (reaction (5)) and OH initiated oxidation (reaction (6)). More details about model setup, $RONO_2$ reactions, and photochemistry of limonene and myrcene are given in Text S1 in the supporting information.

R5 $\quad RONO_2 + h\nu \rightarrow RO + NO_2$

R6 $\quad RONO_2 + OH \rightarrow RO + NO_2 + \text{products}$

The branching ratios were acquired from previous studies (Flocke, Atlas et al., 1998; Lightfoot et al., 1992) or calculated according to the formulas recommended by Carter and Atkinson (1985). For C_1 $RONO_2$, branching ratios of 0.00015, 0.0003, 0.001, 0.003, 0.0041, and 0.005 were examined and considered. The one that resulted in the highest IOA between the simulated and observed C_1 $RONO_2$ was adopted (see section 3.2 for details). However, since branching ratio data for C_2–C_4 $RONO_2$ were rather limited, the values calculated using formulas (1)–(3) were used as the branching ratios, which were 0.0094, 0.048, 0.019, and 0.085 for C_2, 2-C_3, 1-C_3, and 2-C_4 $RONO_2$, respectively.

In addition to the chemical reactions, many modules were compiled in the PBM-MCM model. For example, the photolysis rate module enables us to calibrate the photolysis rates of many air pollutants. The tropospheric ultraviolet and visible radiation model, which considers actual location and modeling time periods, is used to calibrate the photolysis rates (Madronich & Flocke, 1997). Moreover, the concentrations of air pollutants can be specified to initiate the model in the initial concentration module. This is important, because the background $RONO_2$ existed prior to photochemical reactions is generally nonnegligible due to their long lifetimes. The dry deposition module considers the dry deposition of air pollutants, which are parameterized as an average deposition rate within the height of the mixed layer (HMIX).

Since this study mainly focused on the in situ photochemistry of $RONO_2$, the on-site observations of 41 hydrocarbons, 10 halocarbons, 6 OVOCs, 5 inorganic trace gases, and 2 meteorological parameters (temperature and relative humidity) from 08:00 to 19:00 at each site were used as the model input to constrain the modeling (the hourly observed $RONO_2$ at 08:00–19:00 were not input to constrain the simulated $RONO_2$). Moreover, to initiate the modeling, observed concentrations of the aforementioned species including $RONO_2$ at 07:00 were set as initial conditions. These initial conditions were expected to be significantly influenced by regional transport and mesoscale circulation at this mountainous site (because of low on-site emissions). Note that these species were not constrained at their initial values but were allowed to vary over time. Since the daily values of these pollutants varied, different initial concentrations for each pollutant were used for the simulation of each day. The integration of simulated $RONO_2$ within each hour automatically given by the model was compared with the observed $RONO_2$ to validate the model performance. The simulations were carried out only during the daytime hours (07:00–19:00). In terms of dry deposition, Zhang et al. (2002) indicated that the dry deposition velocity for organic nitrates ranged from 0.03 to 0.56/HMIX cm/s (HMIX denotes height of mixed layer). Within this range, deposition rates of 0.03, 0.13, 0.23, 0.33, 0.43, and 0.53/HMIX cm/s were examined for C_1–C_4 $RONO_2$ in this study (step = 0.1/HMIX cm/s). Dry deposition rates were also available for other species such as O_3 and its precursors, in-line with the settings in previous studies (Lam et al., 2013; Saunders et al., 2003).

Overall, based on the observed mixing ratios of air pollutants, including $RONO_2$ precursors, the PBM-MCM model simulated $RONO_2$ in different scenarios with changes of branching ratios and dry deposition rates, and consideration of initial conditions. The model uncertainty was discussed and roughly estimated with the root-mean-square error method (Willmott, 1982) in Text S2 in the supporting information.

3. Results and Discussion

3.1. Overview of $RONO_2$ Sources

As mentioned earlier, the air quality at TMS was significantly influenced by regional transport and mesoscale circulation. Figure S1 shows the distributions of wind fields, that is, wind direction (WD) and wind speed (WS), and their correlations with $RONO_2$ precursors at TMS during the sampling campaign. North winds ($0° < WD < 90°$ and $270° < WD < 360°$) were much more frequent than south winds ($90° < WS < 180°$) at TMS (82.8% and 17.2%, respectively). While the mixing ratios of NO and NO_2 were comparable ($p > 0.05$) for north and south winds, C_1–C_4 *n*-alkanes were more abundant ($p < 0.05$) under north versus south winds, suggesting the transport of $RONO_2$ precursors from the inland PRD to TMS. During this study the average wind direction at TMS switched from northeast at night to north during the day (Guo et al., 2013), implying that regional transport was constant throughout the day or night. Besides regional transport, our previous paper (Guo et al., 2013) clearly confirmed the mesoscale circulations between TMS and TW through the good intersite correlations of SO_2 and CO, good reproduction of O_3 at TMS with precursors at TW to initialize the model, and the simulation of mountain-valley breezes by Weather Research Forecast model. Mesoscale circulations were identified on the sampling days of 24 and 29–31 October and 1–3, 9, and 19 November,

Table 1
Contributions of Regional Transport, Mesoscale Circulation and In Situ Formation to Individual $RONO_2$ Levels at TMS (Unit: pptv) (From Ling et al., 2016)

Sources	CH_3ONO_2	$C_2H_5ONO_2$	2-$C_3H_7ONO_2$	1-$C_3H_7ONO_2$	2-$C_4H_9ONO_2$
Regional transport	7.67 ± 0.50	8.44 ± 0.62	16.86 ± 1.17	2.11 ± 0.22	15.15 ± 1.49
Mesoscale circulation	9.97 ± 0.85	7.38 ± 0.44	18.7 ± 0.77	3.08 ± 0.16	34.7 ± 3.14
In situ formation	3.61 ± 0.48	2.18 ± 0.29	3.68 ± 0.45	1.03 ± 0.13	10.9 ± 1.31

when the valley breeze brought the urban plume at the foot of the mountain to the mountain site in the daytime, while the mountain breeze drove the mountain air to the urban site at night. In addition, the air pollution at TMS was also partially dominated by in situ photochemistry. With the same set of data, Ling et al. (2016) apportioned the observed $RONO_2$ at TMS to the sources of regional transport, mesoscale circulation, and in situ formation, as shown in Table 1. Although regional transport and mesoscale circulation made considerable contributions to $RONO_2$ at TMS, in situ formation cannot be neglected, which was the main focus of this study.

It is well known that photochemical formation, biomass burning, and oceanic emission are the main sources of $RONO_2$ (Atlas et al., 1993; Bertman et al., 1995; Simpson et al., 2002). Using positive matrix factorization model, Ling et al. (2016) resolved the sources of $RONO_2$ at TW (Table 2). Secondary formation (46.6 ± 2.4%) and biomass burning (46.7 ± 2.1%) made comparable contributions to total $RONO_2$, with the rest from oceanic emission (6.8 ± 1.2%). It should be noted that the secondary formation identified by Ling et al. (2016) was not exactly the same as the in situ formation, because the secondarily formed $RONO_2$ in background and regional air masses were also included in the secondary formation source. Further analysis was conducted on the relationship between primarily emitted $RONO_2$ and source origin of air masses. In-line with our previous paper (Guo et al., 2013), the air masses under north winds with WS higher than 2 m/s were treated as regional air. Otherwise, the air masses were local or originated from the South China Sea (SCS). Figure S2 shows the total $RONO_2$ emitted from biomass burning and oceanic emission versus wind fields. $RONO_2$ levels in local air or SCS outflow from both biomass burning (40.0 ± 1.9 pptv) and oceanic emissions (5.4 ± 0.7 pptv) were significantly higher ($p < 0.05$) than in regional air (biomass burning: 35.9 ± 2.2 pptv and oceanic emission: 3.2 ± 1.4 pptv). The higher $RONO_2$ emissions from biomass burning in local air was expected to be caused by biofuel usage in small villages and barbecues nearby (Ling et al., 2016, and references therein). The greater oceanic emissions of $RONO_2$ in local air or SCS outflow indicated the higher oceanic contributions to $RONO_2$ in Hong Kong under south or calm winds (WS < 2 m/s), though we note that the $RONO_2$ levels in the oceanic air are still fairly low (far away from equator).

3.2. Modeling of C_1–C_4 $RONO_2$

3.2.1. Branching Ratio and Deposition Velocity

This study mainly focused on the in situ formation of $RONO_2$ at TMS and TW. However, the regional transport and mesoscale circulation were also partially considered based on the following settings: (i) $RONO_2$ and other air pollutants measured at 07:00 on each day were used to initiate the model; the initial $RONO_2$ at 07:00, which accounted for ~85% of the total simulated $RONO_2$ (see Figure 3), consisted of the regionally transported and locally circulated $RONO_2$; and (ii) the regionally transported and locally circulated fractions of $RONO_2$ precursors were included in the hourly measured data, which were used to construct the model. Despite the above settings, the impacts of regional transport and mesoscale circulations were not fully simulated in the model, demonstrated by the fact that the simulated $RONO_2$ mixing ratios were generally lower than the observed levels during O_3 episodes when these impacts were significant (see Figures S4 and S5),

Table 2
Source Contributions to Individual $RONO_2$ at TW in Different Scenarios (Unit: pptv) (From Ling et al., 2016)

Sources	CH_3ONO_2	$C_2H_5ONO_2$	2-$C_3H_7ONO_2$	1-$C_3H_7ONO_2$	2-$C_4H_9ONO_2$
Secondary formation	4.0 ± 0.3	6.2 ± 0.5	12.1 ± 0.9	2.1 ± 0.2	18.3 ± 1.3
Biomass burning	5.7 ± 0.3	5.7 ± 0.3	12.4 ± 0.6	1.6 ± 0.1	14.2 ± 0.6
Oceanic emission	2.5 ± 0.3	1.1 ± 0.1	1.1 ± 0.1	0.10 ± 0.01	0.4 ± 0.1

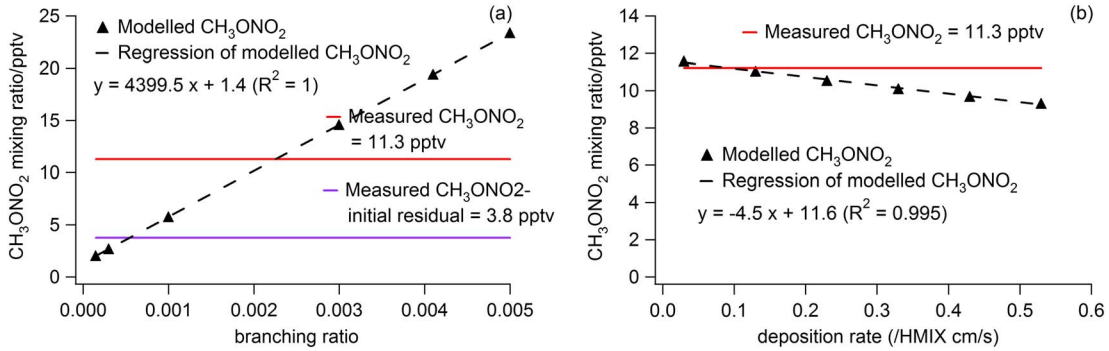

Figure 2. Modeled average CH_3ONO_2 as a function of (a) branching ratio (no initial or dry deposition) and (b) deposition rate (branching ratio = 0.0003, and the initial CH_3ONO_2 was set as the values measured at 07:00 (LT) at TMS for each day.

most likely due to the insufficient consideration of regional transport and local circulation. However, the simulations of in situ formation of $RONO_2$ should not be significantly influenced.

Figure 2a shows the average in situ production of CH_3ONO_2 at TMS as a function of the branching ratio (section 2.3), without consideration of initial concentrations and dry deposition. Noticeably, the CH_3ONO_2 production linearly increases with increasing branching ratio (CH_3ONO_2 mixing ratio in parts per trillion by volume = (4400 × branching ratio) + 1.4). A branching ratio of approximately 0.0023 was determined to match the observed CH_3ONO_2 (11.3 pptv). This branching ratio was within the range of 0.00015 to 0.005 as reported earlier (Carter & Atkinson, 1985; Flocke, Atlas et al., 1998; Lightfoot et al., 1992). However, the initial mixing ratio (8.8 pptv) was not considered in Figure 2a, which should also be a part of the observed CH_3ONO_2 even though it was subject to degradation and dry deposition. Even taking into account the degradation (OH initiated oxidation and photolysis) and dry deposition (rate = 0.13/HMIX cm/s), the average residual of the initial CH_3ONO_2 was still 7.5 pptv. Based on this value, photochemically formed CH_3ONO_2 was about 3.8 pptv, which corresponded to a branching ratio of 0.00055, also within the range of 0.00015–0.005. However, this value was calculated based on model simulation rather than laboratory experiment and has never been reported in previous studies. More importantly, factors other than photochemical reactions (such as regional transport and mesoscale circulation) might influence the determination of this value. Therefore, 0.00055 was only treated as a rough estimate of the branching ratio, and we preliminarily accepted a branching ratio of 0.0003, reported by Flocke, Atlas et al. (1998) and adopted by Simpson et al. (2006), which was the closest to 0.00055 among the examined values.

To validate the suitability of the branching ratio, we conducted a set of comparative simulations with the branching ratios tested above. The initial concentrations were taken from the observed CH_3ONO_2 at 07:00 on each day, and the mean of 0.03/HMIX-0.53/HMIX was set as the dry deposition rate. Table S2 shows the IOAs between the observed and simulated CH_3ONO_2 with different branching ratios. Noticeably, the best agreement was acquired when the branching ratio of 0.0003 was applied. Furthermore, the observed and simulated CH_3ONO_2 with branching ratio of 0.0003 were compared on several selected days with the wind speeds less than 2 m/s and typical patterns of photochemically formed $RONO_2$ (peak observed in earlier afternoon), as presented in Figure S3. It was found that the variations of CH_3ONO_2 were well simulated, with IOA reaching 0.75 at TMS and 0.86 at TW. The average positive and negative biases of the simulations were 18.3% and −12.1% at TMS, and 14.3% and −13.5% at TW, respectively. Under the assumption that the daytime variation of CH_3ONO_2 was exclusively caused by in situ formation on the selected days, the biases of simulations could be treated as the errors in branching ratio, because CH_3ONO_2 production linearly correlated with the branching ratio (Figure 2). By setting the initial concentration and deposition velocity as zero, the average contribution of photochemical formation to the total simulated CH_3ONO_2 on the selected days was determined to be ~44% and ~34% at TMS and TW, respectively. Therefore, to count the maximum biases of the simulated CH_3ONO_2 (18.3% at TMS and

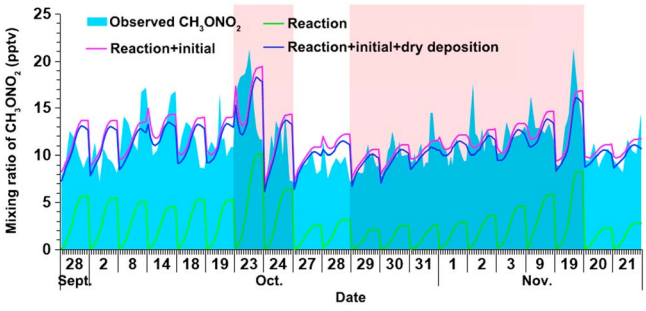

Figure 3. Comparisons between the measured and modeled CH_3ONO_2 in different scenarios at TMS. The O_3 episode days are highlighted in red.

Table 3
Model Settings for the Simulations of C_1–C_4 $RONO_2$ As Well As IOAs Between the Simulated and Measured $RONO_2$ at TMS and TW

	CH_3ONO_2	$C_2H_5ONO_2$	1-$C_3H_7ONO_2$	2-$C_3H_7ONO_2$	2-$C_4H_9ONO_2$
Branching ratio	0.0003	0.0094	0.019	0.048	0.085
Dry deposition	0.07/HMIX	0.07/HMIX	0.07/HMIX	0.07/HMIX	0.07/HMIX
IOA at TMS	0.67	0.72	0.72	0.72	0.72
IOA at TW	0.66	0.70	0.69	0.67	0.73

Note. HMIX is the time-dependent mixed layer height, as shown in Figure S6.

14.3% at TW), the uncertainty of the branching ratio was ~42% at both sites. Further consideration of the model uncertainty (~13%) with the root-mean-square error method (see Text S2) resulted in the uncertainty of the branching ratio less than 50%. Therefore, 0.0003 was identified as the most appropriate branching ratio for $CH_3O_2 + NO \rightarrow CH_3ONO_2$, with the error less than 20%. It is noticeable that 0.00055 was beyond the range of 0.00015–0.00045 (0.0003 with uncertainty of 50%). This discrepancy might be caused by the fact that the determination of 0.00055 was more influenced by the factors other than photochemical reactions, while 0.0003 was determined based on the simulations on the selected days when in situ photochemical formation of CH_3ONO_2 was more significant.

Although 0.0003 was proposed and adopted in some previous studies (Flocke, Atlas et al., 1998; Simpson et al., 2006), other branching ratios over a wide range (0.00015–0.01) have also been used as the branching ratio of CH_3O_2 reacting with NO (e.g., Carter & Atkinson, 1989; Scholtens et al., 1999). Here the determination of the branching ratio of 0.0003 and the associated uncertainty may reconstrain the impacts of CH_3ONO_2 on global oxidative capacity of the atmosphere.

Furthermore, by considering dry deposition, Figure 2b presents the modeled CH_3ONO_2 with the branching ratio of 0.0003 and dry deposition velocities of 0.03/HMIX, 0.13/HMIX, 0.23/HMIX, 0.33/HMIX, 0.43/HMIX, and 0.53/HMIX cm/s. The modeled CH_3ONO_2 decreased linearly with increasing dry deposition velocity (CH_3ONO_2 mixing ratio in pptv = $-4.5 \times$ deposition rate + 11.6). A dry deposition velocity of 0.07/HMIX was determined to best reproduce the observed CH_3ONO_2. As such, the branching ratio of 0.0003 and dry deposition velocity of 0.07/HMIX cm/s were treated as the most appropriate settings for CH_3ONO_2 simulation.

With these settings, the factors influencing the simulated CH_3ONO_2 were sequentially considered. Figure 3 shows the CH_3ONO_2 simulated in different scenarios at TMS, that is, (i) "reaction," (ii) "reaction + initial," and (iii) "reaction + initial + dry deposition." Scenario (i) only considered the formation and degradation reactions of CH_3ONO_2, while the initial concentrations and dry deposition were progressively considered in scenarios (ii) and (iii). The modeled CH_3ONO_2 in scenario (i) was typically bell shaped on a diurnal basis, coincident with the characteristics of photochemical reactions. However, the mean modeled CH_3ONO_2 (2.6 ± 0.3 pptv) was much lower than the observed average (11.3 ± 0.3 pptv). By introducing the initial conditions, the modeled CH_3ONO_2 in scenario (ii) increased to a comparable level (11.7 ± 0.3 pptv) to the measurements, in-line with the finding that background initial concentrations are an important constituent of the observed $RONO_2$ (Ling et al., 2016). Further consideration of dry deposition in scenario (iii) resulted in a slight decrease of the modeled CH_3ONO_2 to 11.0 ± 0.3 pptv, which best agreed with the observed CH_3ONO_2. By subtracting the modeled CH_3ONO_2 in scenario (i) from scenario (ii) and that in scenario (ii) from scenario (iii), the respective contributions of the processes, including reaction, initial conditions, and dry deposition to the total modeled CH_3ONO_2, were determined to be 21.5 ± 1.8%, 85.1 ± 2.0%, and −6.6 ± 0.3% (negative contribution means removal of CH_3ONO_2). It is noteworthy that the initial concentrations included both primarily emitted $RONO_2$ and residues of secondarily formed $RONO_2$ in background and regionally transported air masses. C_2–C_4 $RONO_2$ were simulated with the branching ratios calculated according to Carter and Atkinson (1985, 1989) and the dry deposition velocities identical to that for CH_3ONO_2.

3.2.2. Model Validation

Table 3 lists the model settings that best reproduced the magnitudes and patterns of the observed $RONO_2$ at TMS and TW (shown in Figures S4 and S5 in the supporting information). Overall, the simulated $RONO_2$ agreed well with the measurements (index of agreement is discussed below). However, the morning peaks of $RONO_2$ (e.g., 28 September, 8 and 23 October, and 1 and 2 November) were not well reproduced by the model. Since in situ photochemical formation could not be the main source of $RONO_2$ in the morning

when solar radiation was weak, the discrepancies between modeling and observation were most likely to be caused by direct emissions and/or regional transport, which were not considered in the model. In addition, the modeled $RONO_2$ levels were generally ~50% lower than the observations on O_3 episode days (23–24 and 29–31 October and 1–3, 9, and 19 November). Methyl chloride (CH_3Cl) levels at both TMS (episode: 1100 ± 33 pptv and nonepisode: 926 ± 27 pptv) and TW (episode: 1116 ± 32 pptv and nonepisode: 1031 ± 45 pptv) increased noticeably ($p < 0.05$) during O_3 episodes, so did levoglucosan in fine particles (84.8 ± 27.8 and 31.6 ± 18.5 ng/m^3 during episode and nonepisode at TMS, respectively). These suggested emissions of $RONO_2$ from biomass burning. Furthermore, the frequency of northerly winds was higher during O_3 episodes (78% at TMS and 29% at TW) than during non-O_3 episodes (51% at TMS and 21% at TW). In view of severe photochemical pollution in the adjacent inland PRD cities and increased transport of secondary pollutants from the inland PRD to Hong Kong during O_3 episodes (Guo et al., 2009; Lam et al., 2005), regional transport might also contribute to the higher observed $RONO_2$ on episode days. Additionally, Ling et al. (2016) indicated that mesoscale circulation made higher contribution to $RONO_2$ at TMS during O_3 episodes. An exception was CH_3ONO_2 at TW on 19 November when the modeled CH_3ONO_2 remarkably exceeded the measured values (Figure S5). This overestimation was believed to be caused by the abnormally high aromatic levels on that day (30.2 ± 23.4 ppbv, compared to the average of 4.9 ± 0.6 ppbv over the whole sampling period excluding that day). Briefly, the photochemical degradation of aromatics generated CH_3O_2 and CH_3O in the model. Without consideration of diffusion, these precursors of CH_3ONO_2 were more significantly overestimated than those in normal periods, leading to overestimation of CH_3ONO_2.

To quantitatively evaluate the simulations, IOA between the simulated and observed $RONO_2$ was calculated (Table 3). IOA is a statistical parameter commonly used to evaluate model performance, as calculated using formula (4) (Hurley et al., 2001; Wang et al., 2015). Ranging from 0 to 1, higher IOAs represent better agreement between the simulated and observed values.

$$\mathrm{IOA} = 1 - \frac{\sum_{i=1}^{n} (O_i - S_i)^2}{\sum_{1i=1}^{n} \left(\left| O_i - \overline{O} \right| + \left| S_i - \overline{O} \right| \right)^2}, \tag{4}$$

where O_i and S_i are the observed and simulated values and $\overline{O}$ is the average observed value of n samples.

The IOA ranged from 0.67 to 0.72 and 0.66 to 0.73 for $RONO_2$ simulations at TMS and TW, respectively. Given that other sources (e.g., biomass burning and oceanic emission) and regional transport impact were not considered in the model, the IOAs indicated that the simulations were acceptable.

3.3. Secondary $RONO_2$ Formation

3.3.1. $RONO_2$ Formation at TMS and TW

Based on the above settings, the in situ production of $RONO_2$ (referred to as secondary $RONO_2$ hereafter) was simulated without consideration of initial conditions and dry deposition, as summarized in Table 4. Also shown are the concentrations of parent hydrocarbons, corresponding RO_2 radicals, NO, and NO_2.

The measured mixing ratios of parent hydrocarbons and NO_x (both NO and NO_2) were significantly higher at TW than at TMS ($p < 0.05$). Likewise, simulated C_1 and 2-C_4 $RONO_2$ levels at TW were significantly higher than at TMS ($p < 0.05$), while the simulated C_2 and C_3 $RONO_2$ levels at TW were comparable to or even lower than those at TMS. To explore the reasons for these differences, the relative contributions of RO_2 + NO and RO + NO_2 were quantified (Table 5), using the method described by Lyu et al. (2015). Briefly, the two pathways were switched off in turn. The simulated $RONO_2$ was subtracted from that simulated in base scenario with both pathways switched on. In this way, $RONO_2$ produced by the each pathway was obtained. The pathway of RO_2 + NO dominated the formation of C_2–C_4 $RONO_2$ at both sites. In contrast, the reaction of RO + NO_2 made considerable contributions to CH_3ONO_2 (mean ± 95% confidence interval (CI): 2.7 ± 0.3 pptv or 41.9 ± 5.9% at TMS and 4.8 ± 1.0 pptv or 76.2 ± 15.7% at TW). In addition to higher CH_4 levels, the more abundant secondary CH_3ONO_2 at TW was likely because that NO_2 at TW (31.6 ± 3.1 ppbv) was significantly higher than that at TMS (8.7 ± 0.8 ppbv) ($p < 0.05$). Indeed, following suggestions that RO + NO_2 could be an important pathway for CH_3ONO_2 formation in polluted environments (Flocke, Volz-Thomas et al., 1998; Simpson et al., 2006), Archibald et al. (2007) confirmed that this pathway becomes important at about 10 ppb of NO_2, and dominant at about 35 ppb, based on MCM simulations for European conditions. It is noteworthy

Table 4
Average Mixing Ratios of Parent Hydrocarbons, NO_x, and Secondary $RONO_2$ at TMS and TW

	TMS	TW
CH_4 (ppbv)	1950 ± 7	1970 ± 7
C_2H_6 (pptv)	1848 ± 76	2144 ± 81*
C_3H_8 (pptv)	1123 ± 71	3343 ± 331*
***n*-C_4H_{10} (pptv)**	887 ± 84	4131 ± 361*
NO (ppbv)	3.5 ± 0.1	26.9 ± 2.9*
NO_2 (ppbv)	8.7 ± 0.8	31.6 ± 3.1*
CH_3O_2 (molecules/cm^3)	$(3.1 \pm 0.4) \times 10^7$*	$(0.6 \pm 0.3) \times 10^7$
$C_2H_5O_2$ (molecules/cm^3)	$(2.0 \pm 0.2) \times 10^6$*	$(0.3 \pm 0.1) \times 10^6$
2-$C_3H_7O_2$ (molecules/cm^3)	$(4.6 \pm 0.5) \times 10^5$*	$(0.7 \pm 0.2) \times 10^5$
1-$C_3H_7O_2$ (molecules/cm^3)	$(4.0 \pm 0.6) \times 10^5$*	$(0.3 \pm 0.1) \times 10^5$
2-$C_4H_9O_2$ (molecules/cm^3)	$(7.1 \pm 0.8) \times 10^5$*	$(1.7 \pm 0.5) \times 10^5$
Secondary CH_3ONO_2 (pptv)	2.7 ± 0.3	4.8 ± 1.0*
Secondary $C_2H_5ONO_2$ (pptv)	4.0 ± 0.4	3.6 ± 0.7
Secondary 2-$C_3H_7ONO_2$ (pptv)	5.2 ± 0.5	4.5 ± 0.7
Secondary 1-$C_3H_7ONO_2$ (pptv)	1.1 ± 0.1*	0.7 ± 0.1
Secondary 2-$C_4H_9ONO_2$ (pptv)	13.5 ± 1.4	17.6 ± 2.4*

Note. Error bars represent 95% CIs. *Significant difference between the two sites ($p < 0.05$). Bolded are species with observed values, and the rest are simulated values. *Note.* Error bars represent 95% CIs.

that the in situ contributions of $CH_3O + NO_2$ to CH_3ONO_2 at both sites in the present study were much higher than those simulated in our previous studies (Ling et al., 2016; Lyu et al., 2015), which considered the dispersion and transport of air masses. This was mainly due to the fact that air masses containing NO_2 during the dispersion and transport were diluted based on the model setup in previous studies. Therefore, the simulated contribution of CH_3O+NO_2 pathway was lower in the previous studies when NO_2 concentration was reduced.

For C_2–C_3 $RONO_2$, although the measured parent hydrocarbons were less abundant at TMS than at TW, the simulated concentrations of RO_2 radicals were all remarkably higher under low NO_x conditions but still in VOC-limited regime (as discussed below), leading to comparable (for $C_2H_5ONO_2$ and 2-$C_3H_7ONO_2$) or even higher (for 1-$C_3H_7ONO_2$) mixing ratios of $RONO_2$ at TMS. The difference in NO_x levels was considered to be the main cause of the anticorrelation between the parent hydrocarbons and related RO_2 radicals. As O_3 formation is generally limited by VOCs at both sites (Guo et al., 2013; Ling et al., 2014), the reaction chains of O_3 formation were terminated by NO_x reacting with reactive radicals. Figure S7 shows that the simulated OH and HO_2 levels were much lower at TW than at TMS. This is because the higher NO_x at TW consumed more oxidative substances (e.g., O_3) and radicals (OH and HO_2). Consequently, reactions including the oxidation of parent hydrocarbons at TW were more suppressed, leading to lower production of RO_2 radicals.

However, 2-$C_4H_9ONO_2$ was higher at TW. In addition to the role of NO as the reactant, this was also attributable to the fact that the concentration of 2-$C_4H_9O_2$ at TW was lower than at TMS only by a factor of 4.2, compared to 6.7, 6.6, and 13.3 for $C_2H_5O_2$, 2-$C_3H_7O_2$, and 1-$C_3H_7O_2$, respectively.

Table 5
Relative Contributions (%) of the RO_2 + NO and RO + NO_2 Pathways to $RONO_2$ at TMS and TW

	TMS		TW	
$RONO_2$	RO_2 + NO	RO + NO_2	RO_2 + NO	RO + NO_2
CH_3ONO_2	58.1 ± 6.8	41.9 ± 5.9	23.8 ± 4.8	76.2 ± 15.7
$C_2H_5ONO_2$	99.0 ± 13.4	1.0 ± 0.2	95.8 ± 24.2	4.2 ± 1.2
2-$C_3H_7ONO_2$	99.6 ± 12.7	0.4 ± 0.1	98.9 ± 19.4	1.1 ± 0.2
1-$C_3H_7ONO_2$	99.5 ± 12.4	0.5 ± 0.1	98.1 ± 17.8	1.9 ± 0.4
2-$C_4H_9ONO_2$	99.9 ± 14.1	0.10 ± 0.02	99.7 ± 18.4	0.3 ± 0.1

Note. Error bars represent 95% CIs.

3.3.2. $RONO_2$ Formation in Various Environments

To further investigate $RONO_2$ formation in different environments, a total of 196 scenarios was designed for model simulations. The simulations were conducted in daytime hours (07:00–19:00), in which the concentrations of total volatile organic compounds (TVOCs) and NO_x were allowed to evolve over time. The simulated hourly $RONO_2$ during 07:00–19:00 in each scenario of the simulations were averaged to create the corresponding isopleths. $RONO_2$ production was simulated with a matrix of total VOCs (TVOCs) and NO_x ranging from 40 to 560 ppbv and 5 to 70 ppbv, with a consistent scale of 40 ppbv and 5 ppbv, respectively. The ranges of TVOCs and NO_x were chosen to include not only the observed TVOCs and NO_x in the middle of the sequence but also the best representative NO_x-limited and VOC-limited regimes as discussed below. Apart from their mixing ratios, the

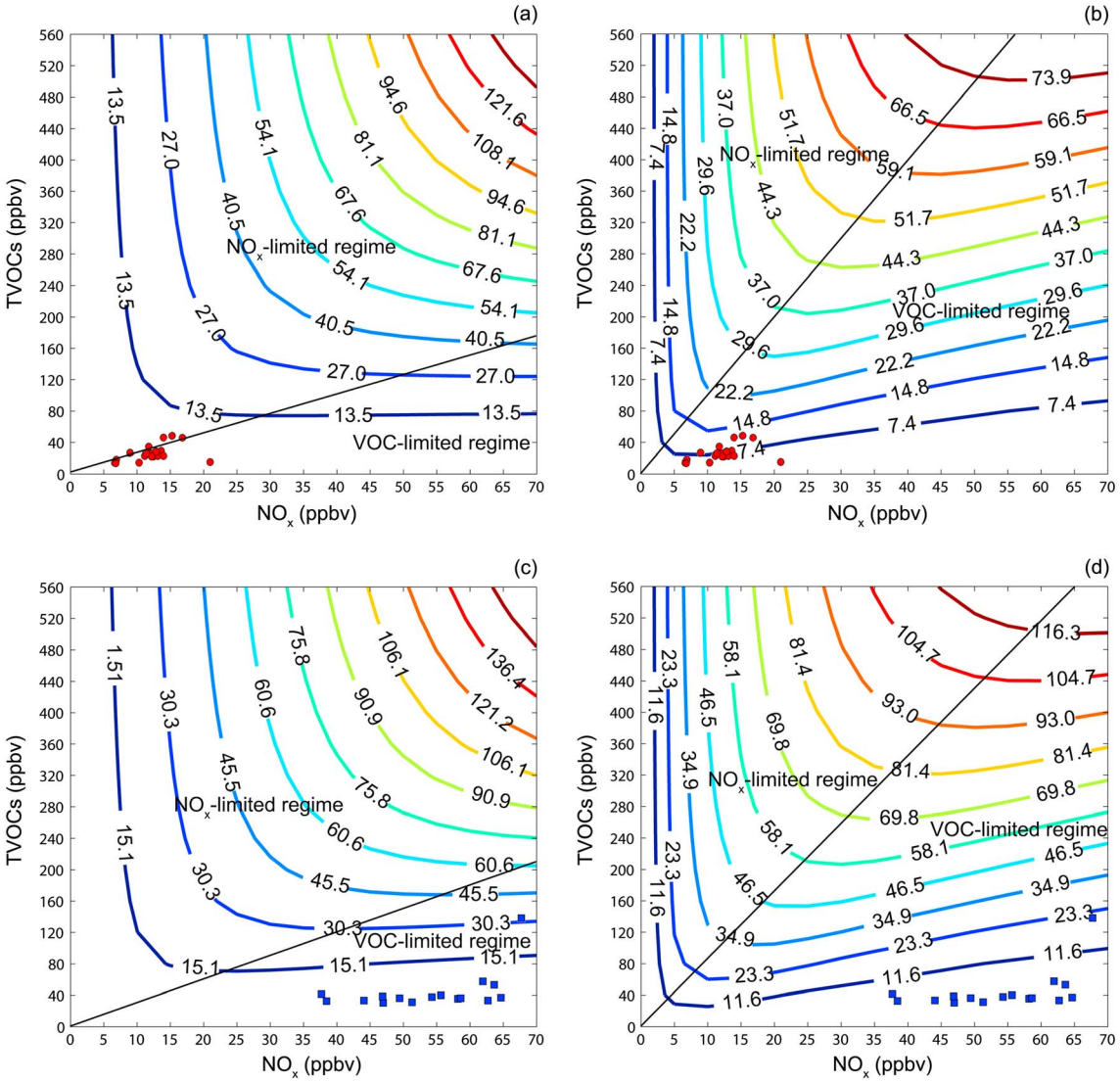

Figure 4. Isopleths of photochemical production (pptv) of (a) CH_3ONO_2 and (b) $C_2H_5ONO_2$ (as an example of C_2–C_4 $RONO_2$) based on the air pollutant profiles at TMS; (c) CH_3ONO_2 and (d) $C_2H_5ONO_2$ (as an example of C_2–C_4 $RONO_2$) based on the air pollutant profiles at TW. The black line separates NO_x-limited regime from VOCs-limited regime. The red and blue symbols in the figure show the daily average observed TVOCs and NO_x at TMS (red) and TW (blue), respectively.

composition of TVOCs and NO_x might also influence the production of $RONO_2$. Therefore, the ratios between VOC species and NO and NO_2 (referred to as air pollutant profiles hereafter) at TMS and TW were used to distribute VOCs species in TVOCs, and NO and NO_2 in NO_x. The mixing ratios of TVOCs and NO_x were 24.0 ± 2.2 and 12.2 ± 0.6 ppbv at TMS and 48.4 ± 7.2 and 50.5 ± 2.3 ppbv at TW, respectively. The ratio of NO_2/NO at TMS (2.5 ± 0.3) was about twice that at TW (1.2 ± 0.2). Further inspection into the OH reactivity indicated that TVOCs and NO_x accounted for ~55% (3.7 s^{-1}) and ~45% (3.0 s^{-1}) of total OH reactivity at TMS. In contrast, the OH reactivity of NO_x at TW (14.3 s^{-1}, ~65%) dominated over that of TVOCs (7.7 s^{-1}, 35%).

Figure 4 shows the isopleths of CH_3ONO_2 and $C_2H_5ONO_2$ production with the changes of TVOCs and NO_x based on the air pollutant profiles at TMS (a and b) and TW (c and d). The isopleth of $C_2H_5ONO_2$ production was selected as an example of C_2–C_4 $RONO_2$, which had the same pattern variations in response to the changes of TVOCs and NO_x (see Figure S8). It is noteworthy that both formation pathways of RO_2 + NO and RO + NO_2 were considered for C_1–C_4 $RONO_2$. Based on Figure 4, the NO_x-limited and VOC-limited regimes in $RONO_2$ formation were identified. Briefly, the points with the lowest TVOCs on each isopleth line were linked in a straight line (dividing line), and $RONO_2$ formation in the area below and above the line was limited by VOCs and NO_x, respectively (Ou et al., 2016). Linear regressions were carried out for these dividing

lines and a TVOC/NO_x ratio of approximately 10.0 ± 0.4 ppbv/ppbv (R^2 = 0.97) was obtained for the simulated production of C_2–C_4 $RONO_2$ based on the air pollutant profiles at TMS. In other words, when the ratio of TVOCs/NO_x was higher (lower) than 10.0 ± 0.4 ppbv/ppbv, the C_2–C_4 $RONO_2$ formation was limited by NO_x (VOCs). However, this ratio was significantly ($p < 0.05$) lower based on the air pollutants profiles at TW (TVOCs/NO_x = 8.7 ± 0.4 ppbv/ppbv, R^2 = 0.96). The differences were likely attributable to the higher fraction of NO_2 in NO_x at TMS (70.6 ± 2.4%) than at TW (54.0 ± 4.1%). NO_2 reacts with OH more quickly than NO, which serves as an important sink of OH in the VOC-limited regime. A higher fraction of NO_2 in NO_x meant that the system was more NO_x suppressed (VOC limited), and a higher ratio of TVOCs/NO_x was needed to change the $RONO_2$ formation from a VOC-limited regime to a NO_x-limited regime. When using OH reactivity to present the dividing ratios, the ratios of $\frac{\text{OH reactivity of TVOCs}}{\text{OH reactivity of NOx}}$ between TMS (6.4 ± 0.3 s^{-1}/s^{-1}) and TW (5.6 ± 0.3 s^{-1}/s^{-1}) were still not comparable ($p < 0.05$). This might be due to the fact that O_3 formation was not only determined by the reactions between OH and VOCs (NO_x). For example, the reaction of NO and OH cannot be treated as a destruction to O_3 in daytime, because OH can be regenerated through the photolysis of HONO. In addition, the same reactivity of TVOCs might correspond to different potentials of O_3 formation, due to the different potentials of RO_2 in oxidizing NO and regenerating HO_2. Analysis of the relationship between $RONO_2$ production and the TVOC/NO_x ratio found that in the NO_x-limited regime, increasing NO_x stimulated the production of $RONO_2$ ($RO_2 + NO \rightarrow RONO_2$). However, increasing NO_x led to a direct or indirect reduction of OH ($OH + NO_2 \rightarrow HNO_3$ and $NO + O_3 \rightarrow NO_2 + O_2$) and subsequent reductions of HO_2, RO_2, and RO in the VOC-limited regime. Conversely, an increase of TVOCs elevated the production of these radicals. Therefore, in the VOC-limited regime, an increase of TVOCs (NO_x) resulted in an increase (decrease) of RO_2, subsequently stimulating (suppressing) $RONO_2$ formation.

Note that the threshold ratios of TVOC/NO_x turning to VOC limited were lower for CH_3ONO_2 formation than for C_2–C_4 $RONO_2$ at both TMS and TW, which were around 2.4 ± 0.2 ppbv/ppbv (R^2 = 0.96) and 3.1 ± 0.1 ppbv/ppbv (R^2 = 0.99) based on the air pollutant profiles at TMS and TW, respectively. In contrast to C_2–C_4 $RONO_2$, which were mainly generated from RO_2 reacting with NO, CH_3ONO_2 had two pivotal formation pathways, that is, $RO_2 + NO$ and $RO + NO_2$ (Table 5). Figures 5a and 5b show the respective isopleths of CH_3ONO_2 produced by the pathways of $CH_3O_2 + NO$ and $CH_3O + NO_2$ based on the air pollutant profiles at TMS (the isopleths at TW are presented in Figures 5c and 5d). The CH_3ONO_2 generated by $CH_3O_2 + NO$ (Figures 5a and 5c) followed the same patterns as C_2–C_4 $RONO_2$ (TVOCs/NO_x ratio of 10.0 ± 0.4 and 8.7 ± 0.4 ppbv/ppbv as the threshold between the VOC- and NO_x-limited regimes at TMS and TW, respectively). However, based on the air pollutants profiles at TMS, the formation of CH_3ONO_2 from the CH_3O+NO_2 always increased with increasing NO_x, implying a continuous NO_x-limited regime. In contrast, NO_x facilitated the pathway of $CH_3O + NO_2 \rightarrow CH_3ONO_2$ when TVOC/NO_x was higher than 2.9 ± 0.1 ppbv/ppbv, based on the air pollutants profiles at TW. The VOC-limited regime under condition of TVOCs/NO_x < 2.9 ± 0.1 ppbv/ppbv was due to the inhabitation of CH_3O formation by NO_x. The production of CH_3ONO_2 through this pathway depended upon the product of CH_3O and NO_2. Since TW had lower fraction of NO_2 in NO_x, the decrease of CH_3O with NO_x increasing cannot be compensated by NO_2 increasing, causing a VOC-limited regime for the pathway of $CH_3O + NO_2$. Moreover, for the scenarios with TVOCs ≥ 240 ppbv, CH_3ONO_2 generated from $CH_3O + NO_2$ continuously increased with increasing NO_x (continuous NO_x-limited regime). The continuous stimulation effect of NO_x on CH_3ONO_2 formation at low ratios of TVOC/NO_x (high NO_x) was also identified by Archibald et al. (2007), which might be caused by the competitiveness of NO_2 associating with CH_3O relative to the oxidation of CH_3O ($CH_3O + O_2 \rightarrow HCHO + HO_2$) increasing under high NO_x. Since RO reacting with NO_2 was an important pathway for C_1 $RONO_2$, a higher fraction of NO_2 in NO_x at TMS meant a higher production of C_1 $RONO_2$ through this route. Therefore, the NO_x-limited regime appeared under conditions of lower ratios of TVOCs/NO_x at TMS.

It should be noted that the aforementioned dividing ratios were obtained based on the average air pollutants profile at each site. In fact, the dividing ratios should vary in a range, due to the change of air pollutant profiles. To further confirm the influence of air pollutant profiles on the dividing ratios, $RONO_2$ formation isopleths were simulated based on the air pollutant profiles at TMS and TW on 9 November 2010, when the air pollutants profiles at TMS and TW were obviously different. Details are given in Text S3 and Table S3 in the supporting information. Noticeably, the distinctive air pollutant profiles on 9 November led to completely different dividing ratios of TVOCs/NO_x from the average ratios. Table 6 lists the ranges of TVOC/NO_x ratios

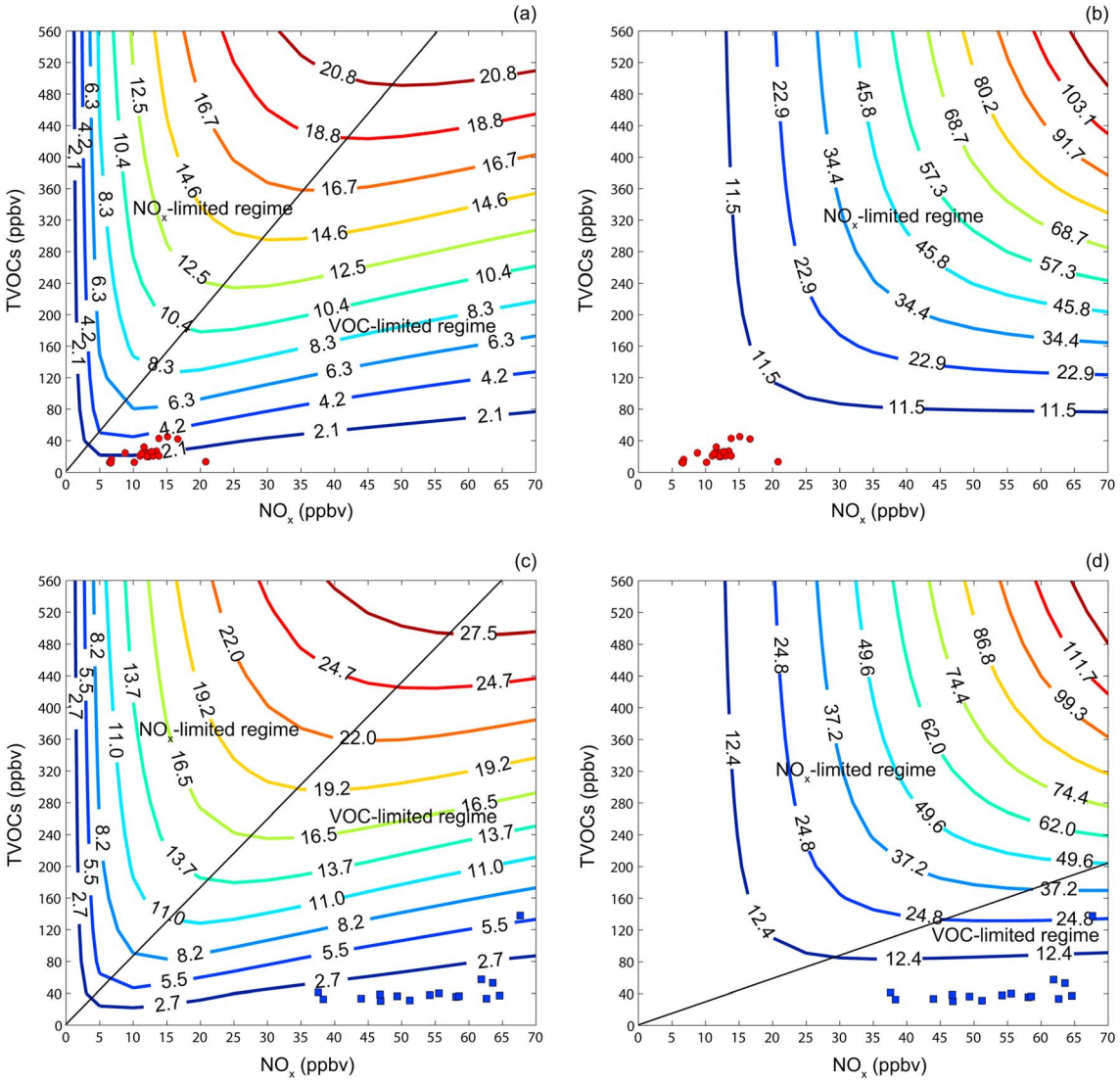

Figure 5. Isopleths of CH_3ONO_2 production (pptv) from the pathway of (a) CH_3O_2+NO and (b) CH_3O+NO_2 based on the air pollutant profiles at TMS; (c) CH_3O_2+NO and (d) CH_3O+NO_2 based on the air pollutant profiles at TW. The red and blue symbols in the figure show the daily average observed TVOCs and NO_x at TMS (red) and TW (blue), respectively.

corresponding to the NO_x-limited and VOCs-limited regimes in $RONO_2$ formation, which were simulated on the basis of the air pollutant profiles at TMS and TW. Please note that these values were the slopes derived from linear regressions. The uncertainty of model simulation was roughly estimated by root-mean-square of the accuracies of input parameters, which was ~13%.

The ratios of TVOCs/NO_x that divide NO_x- and VOC-limited regimes were verified by the observed secondary $RONO_2$, which were resolved by positive matrix factorization model. Details about the source apportionment of $RONO_2$ have been provided in Ling et al. (2016). Figure S9 shows the relationships between the secondary $RONO_2$ and the ratio of TVOCs/NO_x. The samples were grouped using the dividing ratios of TVOCs/NO_x listed in Table 6 to categorize them into the theoretically VOC-limited and NO_x-limited regimes (Figure S9). C_2 $RONO_2$ was selected as an example of C_2–C_4 $RONO_2$, as they all had similar patterns with changing TVOCs/NO_x. Both C_1 and C_2 $RONO_2$ increased with increasing TVOCs/NO_x in the VOC-limited regime and decreased with increasing TVOCs/NO_x in the NO_x-limited regime (not applicable to C_2–C_4 $RONO_2$ since only one sample was in NO_x-limited regime). In other words, the relationships between secondary $RONO_2$ resolved from the observational data and their precursors followed the patterns predicted by $RONO_2$ formation isopleths.

Table 6
Ranges of TVOC/NO_x Ratios Corresponding to Regimes Controlling $RONO_2$ Formation Based On the Air Pollutant Profiles at TMS and TW

TVOCs/NO_x (ppbv/ppbv)	Profiles of air pollutants at TMS		Profiles of air pollutants at TW	
	NO_x limited	VOC limited	NO_x limited	VOC limited
CH_3ONO_2[a]	>2.4 ± 0.2	<2.4 ± 0.2	>3.1 ± 0.1	<3.1 ± 0.1
CH_3ONO_2[b]	>10.0 ± 0.4	<10.0 ± 0.4	>8.7 ± 0.4	<8.7 ± 0.4
CH_3ONO_2[c]	All ratios	None	>2.9 ± 0.1	<2.9 ± 0.1
C_2–C_4 $RONO_2$	>10.0 ± 0.4	<10.0 ± 0.4	>8.7 ± 0.4	<8.7 ± 0.4

[a]Total CH_3ONO_2 produced by CH_3O_2 + NO and CH_3O + NO_2. [b]CH_3ONO_2 produced by CH_3O_2 + NO. [c]CH_3ONO_2 produced by CH_3O + NO_2.

3.4. Impacts on O_3 Production

3.4.1. O_3 Variation Induced by $RONO_2$ Formation at TMS and TW

To investigate the impacts of $RONO_2$ formation on O_3 production, two categories of scenarios, that is, a base case and five constrained cases, were tested for each sampling day in this study. Briefly, in the base case all reaction pathways were switched on in the model, while the formation pathways (RO_2 + NO and RO + NO_2) of each individual $RONO_2$ were switched off in each corresponding constrained case. The five constrained cases corresponded to five $RONO_2$. All other settings were identical between the base and constrained cases. The initial concentrations of C_1–C_4 $RONO_2$ were set as zero for both the base and constrained cases, because we focused on the impacts of in situ $RONO_2$ formation on O_3 production. The base case simulated the secondary production of $RONO_2$. The O_3 variations (ΔO_3) induced by $RONO_2$ formation were obtained by subtracting O_3 in the constrained cases from that in the base case, as were the variations of NO, NO_2, OH, and HO_2. Figure 6 shows the relationship between hourly ΔO_3 and secondary $RONO_2$ production at TMS and TW using all measured data points for the whole sampling period. Each point denotes hourly simulated O_3 reduction induced by $RONO_2$ formation in that hour. Overall, as secondary $RONO_2$ production increased, O_3 levels decreased. The formation of CH_3ONO_2, $C_2H_5ONO_2$, 2-$C_3H_7ONO_2$, 1-$C_3H_7ONO_2$, and 2-$C_4H_9ONO_2$ caused an average O_3 reduction (mean ± 95% CI) of 9.7 ± 1.1, 14.7 ± 1.6, 18.4 ± 1.9, 6.9 ± 0.6, and 60.2 ± 6.8 pptv at TMS, and 10.5 ± 3.2, 7.1 ± 2.0, 8.3 ± 2.1, 2.0 ± 0.5, and 40.0 ± 9.8 pptv at TW, respectively. Note that these values were different from those reported at the same sites in Ling et al. (2016), which considered both $RONO_2$ formation on site and during mesoscale circulation. O_3 reduction was linearly correlated with the production of secondary $RONO_2$ ($0.72 < R^2 < 0.95$ at TMS, $0.77 < R^2 < 0.84$ at TW) for CH_3ONO_2, $C_2H_5ONO_2$, 2-$C_3H_7ONO_2$, 1-$C_3H_7ONO_2$, and 2-$C_4H_9ONO_2$, respectively. Furthermore, the daily average O_3 reduction correlated well with the reduction of OH (R^2 = 0.83 and 0.71 at TMS and TW, respectively) and of HO_2 (R^2 = 0.84 and 0.98 at TMS and TW, respectively), while poor correlations were found between O_3 reduction and the variation of NO or NO_2 (Figures S10 and S11). This was consistent with our previous finding that O_3 reduction in $RONO_2$ formation was related to the reductions of oxidative radicals in VOC-limited regime (Lyu et al., 2015). More

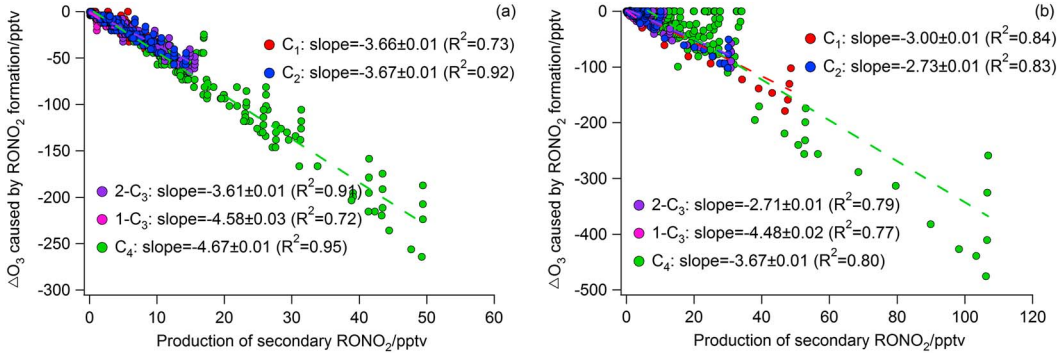

Figure 6. Relationship between O_3 reductions and the simulated secondary $RONO_2$ productions at (a) TMS and (b) TW.

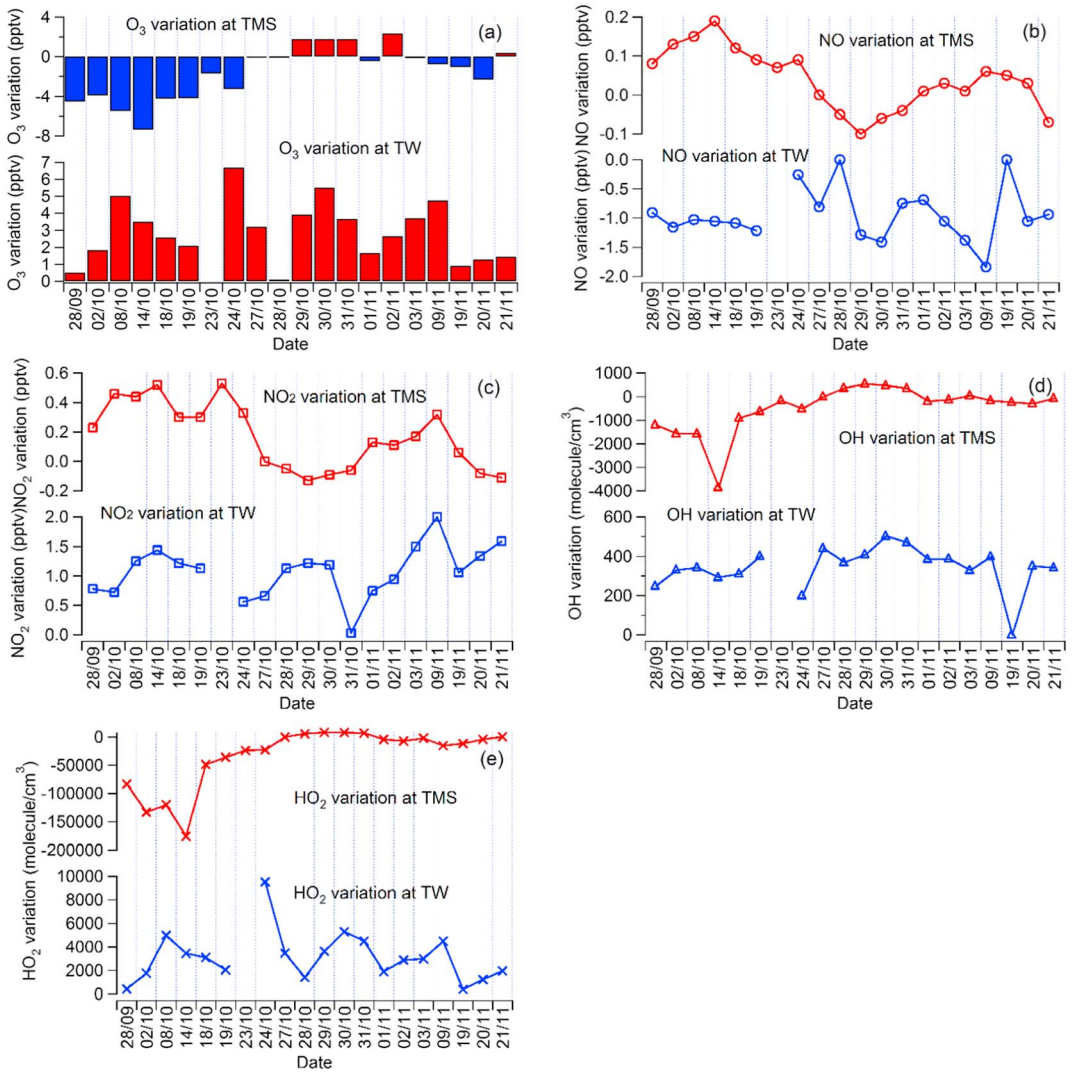

Figure 7. Simulated variations of (a) O_3, (b) NO, (c) NO_2, (d) OH, and (e) HO_2 at TMS and TW induced by C_1–C_4 $RONO_2$ degradation.

importantly, the O_3 reduction efficiencies (ΔO_3/secondary $RONO_2$) were significantly lower at TW than at TMS ($p < 0.05$), as reflected from the slopes in Figure 6. In view of the higher OH and HO_2 at TMS than at TW (Figure S7), the higher O_3 reduction efficiency at TMS suggested that $RONO_2$ formation led to O_3 reduction more significantly in the atmosphere with higher oxidative capacity. This is reasonable because the promotion of OH and HO_2 to the propagation of chain reactions forming O_3 is faster in the more oxidative atmosphere. This finding should be applicable to the regions where O_3 formation is limited by VOCs.

3.4.2. O_3 Variation Induced by $RONO_2$ Degradation at TMS and TW

The impacts of $RONO_2$ degradation on O_3 production at TMS and TW were studied with two simulation scenarios, that is, a base scenario with all the reaction pathways switched on and a constrained scenario in which OH oxidation and photolysis for all five C_1–C_4 $RONO_2$ were switched off. The differences of model output between the two scenarios (base scenario-constrained scenario) reflected the impact of $RONO_2$ degradation, referred to as "variation" hereafter. For example, positive variations of O_3 meant that O_3 increased due to $RONO_2$ degradation. Note that this impact was studied in the form of total C_1–C_4 $RONO_2$ rather than individual species, because the O_3 variation induced by individual $RONO_2$ was generally minor. During $RONO_2$ degradation NO_2 is released, which decomposes and generates NO and O, allowing O_3 to be formed through the association between O_2 and O. On the other hand, the released NO_2 also consumes OH, reducing O_3

production subsequently. RO released from $RONO_2$ degradation fuels O_3 formation. Therefore, O_3 variation in $RONO_2$ degradation is the combination of these effects.

Figure 7 shows the simulated daily average variations of O_3, NO, NO_2, OH, and HO_2 induced by degradation of the C_1–C_4 $RONO_2$. The daily average O_3 variations ranged from −7.4 pptv to 2.3 pptv at TMS but increased at TW throughout the sampling campaign (average increase of 2.9 ± 0.8 pptv). At TMS, the O_3 variation correlated well with the OH and HO_2 variations (R^2 of 0.86 and 0.85, respectively) but negatively with the variations of NO and NO_2 (R^2 of 0.89 and 0.76, respectively). This implied that O_3 formation at TMS was generally VOC limited (NO_x suppressed). When NO and NO_2 levels increased at TMS, O_3, OH, and HO_2 decreased. This might be due to the consumption of OH by NO_2 and/or NO titration with O_3. Since NO increases resulted from the decomposition of NO_2, we defined this impact of $RONO_2$ degradation on O_3 production as NO_2 suppressing. In contrast, O_3 formation was enhanced by $RONO_2$ degradation on several days (29–31 October and 2 and 21 November), when NO and NO_2 decreased (due to increases of O_3 and OH) while OH and HO_2 increased. That is, NO_x led to an O_3 reduction. Conversely, RO released from $RONO_2$ promoted O_3 formation. The overall O_3 enhancements indicated that the RO stimulating effect overrode the NO_2 suppressing effect in these cases, causing an O_3 increase. Thus, the impact of $RONO_2$ degradation on O_3 production manifested as RO stimulating. Consistently, O_3, OH and HO_2 all increased while NO decreased at TW, induced by $RONO_2$ degradation. O_3 enhancement exhibited moderate to good correlations with the simulated increase of OH (R^2 = 0.50) and HO_2 (R^2 = 0.81), which were generated from the evolution of RO in the photochemical reaction chain. As such, the impact of $RONO_2$ degradation on O_3 production at TW was dominated by the effect of RO stimulating. We found that the ratio of TVOC/NO_x in the cases of O_3 increase (average: 1.6 ppbv/ppbv) was lower than in the cases of O_3 decrease (average ratio: 2.1 ppbv/ppbv) at TMS. The lower ratio of TVOC/NO_x means that O_3 formation was more limited by VOCs, which enabled the added RO to more efficiently stimulate O_3 formation and resulted in the increase of O_3. Coincidently, the low ratio of TVOC/NO_x (0.9 ppbv/ppbv) at TW also caused O_3 increase during $RONO_2$ degradation.

Further, Text S4 and Figures S12–S14 in the supporting information present the impacts of $RONO_2$ degradation on O_3 production in different environments, through 196 scenarios of simulation. NO_2 released from $RONO_2$ degradation was found to promote O_3 production in NO_x-limited regime, which was defined as NO_2 stimulating effect. Due to the long lifetimes of C_1–C_4 $RONO_2$ and their abundances in specific environments, for example, up to 50 pptv for CH_3ONO_2 within the marine boundary layer near equator (Blake et al., 1999), the degradation of C_1–C_4 $RONO_2$ might cause greater O_3 variations, particularly in pristine environments with sparse emission of O_3 precursors.

4. Conclusions

A PBM-MCM model was developed to simulate gas-phase $RONO_2$ measured at an urban and a mountainous site in Hong Kong. The magnitudes and variations of the observed C_1–C_4 $RONO_2$ at both sites were well reproduced by the model. A branching ratio of 0.0003 with the uncertainty of less than 50% was determined for the reaction of CH_3O_2 + NO leading to CH_3ONO_2 formation, which would be an important reference for modeling the global oxidative capacity of the atmosphere. The modeling results indicated that $RONO_2$ formation depended upon not only the abundances of precursors but also the concentrations of oxidative radicals, which was closely related to the levels of VOCs and NO_x. Although the precursors of $RONO_2$ at the mountainous site were less abundant than at the urban site, the higher concentrations of oxidative radicals led to higher production of RO_2 radicals, resulting in comparable or even higher $RONO_2$. The regimes in which the formation of C_2–C_4 $RONO_2$ was NO_x limited and VOC limited were identified when the ratio of TVOCs/NO_x was higher and lower than 10.0 ± 0.4 ppbv/ppbv, respectively, based on the air pollutants profiles at the mountainous site. The simulated dividing ratio of TVOCs/NO_x based on the air pollutants profiles at the urban site was slightly lower (8.7 ± 0.4 ppbv/ppbv), due to the differences in air pollutant profiles at these two sites. However, the dividing ratios decreased to 2.4 ± 0.2 and 3.1 ± 0.1 ppbv/ppbv for the formation of CH_3ONO_2 at the mountainous and urban site, respectively. This was mainly because CH_3ONO_2 produced from CH_3O + NO_2 continued to increase with increasing NO_x when the ratios of TVOCs/NO_x were relatively low (high NO_x). $RONO_2$ formation generally resulted in O_3 reductions, and the O_3 reduction efficiency was higher at the mountainous site due to the higher oxidative capacity of the atmosphere. On the other

hand, the mechanisms of $RONO_2$ degradation influencing O_3 production included NO_2 stimulating, NO_2 suppressing, and RO stimulating processes. At the mountainous site, the impact of $RONO_2$ degradation on O_3 production was dominated by NO_2 suppression under the condition of relatively high ratios of TVOCs/NO_x, leading to the decrease of O_3, while RO stimulation occurred at relatively low ratios of TVOCs/NO_x, resulting in the increase of O_3. However, the O_3 production always increased due to RO stimulation at the urban site.

Acknowledgments
This study was supported by the Research Grants Council of the Hong Kong Special Administrative Region via grants PolyU5154/13E, PolyU152052/14E, PolyU152052/16E, CRF/C5004-15E, and CRF/C5022-14G, the Research Institute for Sustainable Urban Development of Hong Kong Polytechnic University (1-BBW4), and the Hong Kong Polytechnic University PhD scholarships (project RTUP). This study is partly supported by the Hong Kong PolyU internal grant (G-YBHT, 1-ZVJT, and 4-ZZFW) and the National Natural Science Foundation of China (41275122). The data are accessible at https://drive.google.com/file/d/0B0r5QxfKPoyUYTNyNUctcWNaeTg/view?usp=sharing.

References

Archibald, A. T., Khan, M. A. H., Watson, L. A., Clemitshaw, K. C., Utembe, S. R., Jenkin, M. E., & Shallcross, D. E. (2007). Comment on "Long-term atmospheric measurements of C_1–C_5 alkyl nitrates in the Pearl River Delta region of southeast China" by Simpson et al. *Atmospheric Environment*, *41*(34), 7369–7370.

Arey, J., Aschmann, S. M., Kwok, E. S., & Atkinson, R. (2001). Alkyl nitrate, hydroxyalkyl nitrate, and hydroxycarbonyl formation from the NO_x-air photooxidations of C_5–C_8 *n*-alkanes. *The Journal of Physical Chemistry. A*, *105*(6), 1020–1027.

Aruffo, E., Di Carlo, P., Dari-Salisburgo, C., Biancofiore, F., Giammaria, F., Busilacchio, M., … Stone, D. (2014). Aircraft observations of the lower troposphere above a megacity: Alkyl nitrate and ozone chemistry. *Atmospheric Environment*, *94*, 479–488.

Atkinson, R. (1990). Gas-phase tropospheric chemistry of organic compounds: A review. *Atmospheric Environment. Part A. General Topics*, *24*(1), 1–41.

Atkinson, R., Aschmann, S. M., Carter, W. P., Winer, A. M., & Pitts, J. N. Jr. (1982). Alkyl nitrate formation from the nitrogen oxide (NO_x)-air photooxidations of C_2–C_8 n-alkanes. *The Journal of Physical Chemistry*, *86*(23), 4563–4569.

Atkinson, R., Aschmann, S. M., & Winer, A. M. (1987). Alkyl nitrate formation from the reaction of a series of branched RO_2 radicals with NO as a function of temperature and pressure. *Journal of Atmospheric Chemistry*, *5*(1), 91–102.

Atlas, E., Pollock, W., Greenberg, J., Heidt, L., & Thompson, A. M. (1993). Alkyl nitrates, nonmethane hydrocarbons, and halocarbon gases over the equatorial Pacific Ocean during SAGA 3. *Journal of Geophysical Research*, *98*(D9), 16,933–16,947. https://doi.org/10.1029/93JD01005

Bertman, S. B., Roberts, J. M., Parrish, D. D., Buhr, M. P., Goldan, P. D., Kuster, W. C., … Westberg, H. (1995). Evolution of alkyl nitrates with air mass age. *Journal of Geophysical Research*, *100*(D11), 22,805–22,813. https://doi.org/10.1029/95JD02030

Blake, N. J., Blake, D. R., Wingenter, O. W., Sive, B. C., Kang, C. H., Thornton, D. C., … Rowland, F. S. (1999). Aircraft measurements of the latitudinal, vertical, and seasonal variations of NMHCs, methyl nitrate, methyl halides, and DMS during the First Aerosol Characterization Experiment (ACE 1). *Journal of Geophysical Research*, *104*(D17), 21,803–21,817. https://doi.org/10.1029/1999JD900238

Buhr, M. P., Parrish, D. D., Norton, R. B., Fehsenfeld, F. C., Sievers, R. E., & Roberts, J. M. (1990). Contribution of organic nitrates to the total reactive nitrogen budget at a rural eastern US site. *Journal of Geophysical Research*, *95*(D7), 9809–9816. https://doi.org/10.1029/JD095iD07p09809

Carter, W. P., & Atkinson, R. (1985). Atmospheric chemistry of alkanes. *Journal of Atmospheric Chemistry*, *3*(3), 377–405.

Carter, W. P., & Atkinson, R. (1989). Alkyl nitrate formation from the atmospheric photoxidation of alkanes; a revised estimation method. *Journal of Atmospheric Chemistry*, *8*(2), 165–173.

Clemitshaw, K. C., Williams, J., Rattigan, O. V., Shallcross, D. E., Law, K. S., & Cox, R. A. (1997). Gas-phase ultraviolet absorption cross-sections and atmospheric lifetimes of several C2–C5 alkyl nitrates. *Journal of Photochemistry and Photobiology A: Chemistry*, *102*(2), 117–126.

Colman, J. J., Swanson, A. L., Meinardi, S., Sive, B. C., Blake, D. R., & Rowland, F. S. (2001). Description of the analysis of a wide range of volatile organic compounds in whole air samples collected during PEM-Tropics A and B. *Analytical Chemistry*, *73*(15), 3723–3731.

Darnall, K. R., Carter, W. P., Winer, A. M., Lloyd, A. C., & Pitts, J. N. Jr. (1976). Importance of RO_2 + nitric oxide in alkyl nitrate formation from C_4–C_6 alkane photooxidations under simulated atmospheric conditions. *The Journal of Physical Chemistry*, *80*(17), 1948–1950.

Day, D. A., Dillon, M. B., Wooldridge, P. J., Thornton, J. A., Rosen, R. S., Wood, E. C., & Cohen, R. C. (2003). On alkyl nitrates, O_3, and the "missing NO_y". *Journal of Geophysical Research 108*(D16), 4501. https://doi.org/10.1029/2003JD003685

Farmer, D. K., Perring, A. E., Wooldridge, P. J., Blake, D. R., Baker, A., Meinardi, S., … Cohen, R. C. (2011). Impact of organic nitrates on urban ozone production. *Atmospheric Chemistry and Physics*, *11*(9), 4085–4094.

Flocke, F., Atlas, E., Madronich, S., Schauffler, S. M., Aikin, K., Margitan, J. J., & Bui, T. P. (1998). Observations of methyl nitrate in the lower stratosphere during STRAT: Implications for its gas phase production mechanisms. *Geophysical Research Letters*, *25*(11), 1891–1894. https://doi.org/10.1029/98GL01417

Flocke, F., Volz-Thomas, A., Buers, H. J., Patz, W., Garthe, H. J., & Kley, D. (1998). Long-term measurements of alkyl nitrates in southern Germany: 1. General behavior and seasonal and diurnal variation. *Journal of Geophysical Research*, *103*(D5), 5729–5746. https://doi.org/10.1029/97JD03461

Guo, H., Jiang, F., Cheng, H. R., Simpson, I. J., Wang, X. M., Ding, A. J., … Xie, M. (2009). Concurrent observations of air pollutants at two sites in the Pearl River Delta and the implication of regional transport. *Atmospheric Chemistry and Physics*, *9*(19), 7343–7360.

Guo, H., Ling, Z. H., Cheung, K., Jiang, F., Wang, D. W., Simpson, I. J., … Blake, D. R. (2013). Characterization of photochemical pollution at different elevations in mountainous areas in Hong Kong. *Atmospheric Chemistry and Physics*, *13*(8), 3881–3898.

Hurley, P. J., Blockley, A., & Rayner, K. (2001). Verification of a prognostic meteorological and air pollution model for year-long predictions in the Kwinana industrial region of Western Australia. *Atmospheric Environment*, *35*, 1871–1880.

Jenkin, M. E., Young, J. C., & Rickard, A. R. (2015). The MCM v3.3.1 degradation scheme for isoprene. *Atmospheric Chemistry and Physics*, *15*(20), 11,433–11,459.

Khan, M. A. H., Cooke, M. C., Utembe, S. R., Morris, W. C., Archibald, A. T., Derwent, R. G., … Shallcross, D. E. (2015). Global modeling of the C_1–C_3 alkyl nitrates using STOCHEM-CRI. *Atmospheric Environment*, *123*, 256–267.

Lam, K. S., Wang, T. J., Wu, C. L., & Li, Y. S. (2005). Study on an ozone episode in hot season in Hong Kong and transboundary air pollution over Pearl River Delta region of China. *Atmospheric Environment*, *39*, 1967–1977.

Lam, S. H. M., Saunders, S. M., Guo, H., Ling, Z. H., Jiang, F., Wang, X. M., & Wang, T. J. (2013). Modelling VOC source impacts on high ozone episode days observed at a mountain summit in Hong Kong under the influence of mountain-valley breezes. *Atmospheric Environment*, *81*, 166–176.

Lightfoot, P. D., Cox, R. A., Crowley, J. N., Destriau, M., Hayman, G. D., Jenkin, M. E., … Zabel, F. (1992). Organic peroxy radicals: Kinetics, spectroscopy and tropospheric chemistry. *Atmospheric Environment. Part A. General Topics*, *26*(10), 1805–1961.

Ling, Z. H., Guo, H., Lam, S. H. M., Saunders, S. M., & Wang, T. (2014). Atmospheric photochemical reactivity and ozone production at two sites in Hong Kong: Application of a master chemical mechanism-photochemical box model. *Journal of Geophysical Research: Atmospheres*, *119*(17), 10,567–10,582. https://doi.org/10.1002/2014JD021794

Ling, Z. H., Guo, H., Simpson, I. J., Saunders, S. M., Lam, S. H. M., Lyu, X. P., & Blake, D. R. (2016). New insight into the spatiotemporal variability and source apportionments of C_1–C_4 alkyl nitrates in Hong Kong. *Atmospheric Chemistry and Physics*, *16*, 8141–8156.

Lyu, X. P., Ling, Z. H., Guo, H., Saunders, S. M., Lam, S. H. M., Wang, N., … Wang, T. (2015). Re-examination of C_1–C_5 alkyl nitrates in Hong Kong using an observation-based model. *Atmospheric Environment*, *120*, 28–37.

Madronich, S., & Flocke, S. (1997). Theoretical estimation of biologically effective UV radiation at the Earth's surface. In C. Zerefos (Ed.), *Solar ultraviolet radiation-modeling, measurements and effects* (Vol. I52*NATO ASI Series*) (pp. 23–48). Berlin: Springer-Verlag.

Muthuramu, K., Shepson, P. B., Bottenheim, J. W., Jobson, B. T., Niki, H., & Anlauf, K. G. (1994). Relationships between organic nitrates and surface ozone destruction during Polar Sunrise Experiment 1992. *Journal of Geophysical Research*, *99*(D12), 25,369–25,378. https://doi.org/10.1029/94JD01309

Ou, J., Yuan, Z., Zheng, J., Huang, Z., Shao, M., Li, Z., … Louie, P. (2016). Ambient ozone control in a photochemically active region: Short-term despiking or long-term attainment? *Environmental Science & Technology*, *50*(11), 5720–5728.

Perring, A. E., Bertram, T. H., Farmer, D. K., Wooldridge, P. J., Dibb, J., Blake, N. J., … Sachse, G. (2010). The production and persistence of $\Sigma RONO_2$ in the Mexico City plume. *Atmospheric Chemistry and Physics*, *10*(15), 7215–7229.

Perring, A. E., Pusede, S. E., & Cohen, R. C. (2013). An observational perspective on the atmospheric impacts of alkyl and multifunctional nitrates on ozone and secondary organic aerosol. *Chemical Reviews*, *113*(8), 5848–5870.

Ranschaert, D. L., Schneider, N. J., & Elrod, M. J. (2000). Kinetics of the $C_2H_5O_2$ + NO_x reactions: Temperature dependence of the overall rate constant and the $C_2H_5ONO_2$ branching channel of $C_2H_5O_2$ + NO. *The Journal of Physical Chemistry. A*, *104*(24), 5758–5765.

Roberts, J. M., & Fajer, R. W. (1989). UV absorption cross sections of organic nitrates of potential atmospheric importance and estimation of atmospheric lifetimes. *Environmental Science & Technology*, *23*(8), 945–951.

Rosen, R. S., Wood, E. C., Wooldridge, P. J., Thornton, J. A., Day, D. A., Kuster, W., … Cohen, R. C. (2004). Observations of total alkyl nitrates during Texas Air Quality Study 2000: Implications for O_3 and alkyl nitrate photochemistry. *Journal of Geophysical Research*, *109*. D07303. https://doi.org/10.1029/2003JD004227

Saunders, S. M., Jenkin, M. E., Derwent, R. G., & Pilling, M. J. (2003). Protocol for the development of the master chemical mechanism, MCM v3 (Part A): Tropospheric degradation of non-aromatic volatile organic compounds. *Atmospheric Chemistry and Physics*, *3*(1), 161–180.

Scholtens, K. W., Messer, B. M., Cappa, C. D., & Elrod, M. J. (1999). Kinetics of the CH_3O_2 + NO reaction: Temperature dependence of the overall rate constant and an improved upper limit for the CH_3ONO_2 branching channel. *The Journal of Physical Chemistry. A*, *103*(22), 4378–4384.

Shao, M., Zhang, Y., Zeng, L., Tang, X., Zhang, J., Zhong, L., & Wang, B. (2009). Ground-level ozone in the Pearl River Delta and the roles of VOC and NO_x in its production. *Journal of Environmental Management*, *90*(1), 512–518.

Sillman, S. & He, D. (2002). Some theoretical results concerning O_3-NO_x-VOC chemistry and NO_x-VOC indicators. *Journal of Geophysical Research 107*(D22), 4659. https://doi.org/10.1029/2001JD001123

Simpson, I. J., Meinardi, S., Blake, D. R., Blake, N. J., Rowland, F. S., Atlas, E., & Flocke, F. (2002). A biomass burning source of C_1–C_4 alkyl nitrates. *Geophysical Research Letters 29*(24), 2168. https://doi.org/10.1029/2002GL016290

Simpson, I. J., Wang, T., Guo, H., Kwok, Y. H., Flocke, F., Atlas, E., … Blake, D. R. (2006). Long-term atmospheric measurements of C_1–C_5 alkyl nitrates in the Pearl River Delta region of southeast China. *Atmospheric Environment*, *40*(9), 1619–1632.

Simpson, I. J., Akagi, S. K., Barletta, B., Blake, N. J., Choi, Y., Diskin, G. S., … Blake, D. R. (2011). Boreal forest fire emissions in fresh Canadian smoke plumes: C_1–C_{10} volatile organic compounds (VOCs), CO_2, CO, NO_2, NO, HCN and CH_3CN. *Atmospheric Chemistry and Physics*, *11*, 6445–6463.

Sobanski, N., Schuladen, J., Schuster, G., Lelieveld, J., & Crowley, J. N. (2016). A five-channel cavity ring-down spectrometer for the detection of NO_2, NO_3, N_2O_5, total peroxy nitrates and total alkyl nitrates. *Atmospheric Measurement Techniques*, *9*, 5103–5118.

Thornton, J. A., Wooldridge, P. J., Cohen, R. C., Martinez, M., Harder, H., Brune, W. H., … Fried, A. (2002). Ozone production rates as a function of NO_x abundances and HO_x production rates in the Nashville urban plume. *Journal of Geophysical Research 107*(D12), 4146. https://doi.org/10.1029/2001JD000932

Wang, N., Guo, H., Jiang, F., Ling, Z. H., & Wang, T. (2015). Simulation of ozone formation at different elevations in mountainous area of Hong Kong using WRF-CMAQ model. *Science of the Total Environment*, *505*, 939–951.

Williams, J. E., Le Bras, G., Kukui, A., Ziereis, H., & Brenninkmeijer, C. A. M. (2014). The impact of the chemical production of methyl nitrate from the NO + CH_3O_2 reaction on the global distributions of alkyl nitrates, nitrogen oxides and tropospheric ozone: A global modelling study. *Atmospheric Chemistry and Physics*, *14*(5), 2363–2382.

Willmott, C. J. (1982). Some comments on the evaluation of model performance. *Bulletin of the American Meteorological Society*, *63*(11), 1309–1313.

Zhang, L., Moran, M. D., Makar, P. A., Brook, J. R., & Gong, S. (2002). Modelling gaseous dry deposition in AURAMS: A unified regional air-quality modelling system. *Atmospheric Environment*, *36*(3), 537–560.